Applied Geochemistry 183 (2025) 106323

Contents lists available at ScienceDirect

Applied Geochemistry

journal homepage: www.elsevier.com/locate/apgeochem

Aqueous solubilities in the apatite solid-solution system with double co-substitution on both Ca–Sr cation and OH–F anion sublattice positions

Michael Kersten

Institute of Geosciences, Johannes Gutenberg-University, D-55099, Mainz, Germany

ARTICLE INFO

Editorial handling by: Elisa Sacchi

Keywords:
Strontium
Apatite solubility
Stoichiometric dissolution
Thermodynamic equilibrium
Lippmann diagram

ABSTRACT

To investigate the potential for Sr-90 radionuclide sequestration by apatite phases in contaminated soils and aquifers, the solubility product constants of solid solutions in the apatite supergroup system $(Ca,Sr)_5(PO_4)_3(OH,F)$ were studied. Binary hydroxyl- and fluorapatite solid solutions of varying compositions were synthesized hydrothermally at 200 °C and characterized by using Rietveld and chemical analysis. The lattice axis lengths and cell volumes exhibited a linear increase with increasing Sr content, adhering to Vegard's law and indicating mixing without mixing gaps in the solid-solution system. Dissolution studies were conducted at 25 °C through aqueous batch equilibrium experiments. Aqueous solubility increased with the mole fraction of Sr. However, batch equilibration over weeks led to a stoichiometric rather than a true equilibrium state. Such stoichiometric dissolution of a solid solution is commonly observed in low-solubility phases such as apatite minerals. Stoichiometric saturation for solid solutions corresponds to equal molar Gibbs energy functions of the solid and aqueous phases, which can be represented by an "equal-G curve" (EGC) in Lippmann diagrams. Stoichiometric solubility product constants K_{st} were calculated from the solute activities in the dissolution experiments. These constants align along the straight EGC line connecting the endmember solubility product constants. The excess Gibbs energy of mixing in the solid phase is therefore zero indicating formation of an ideal solid solution system. Correct binary Lippmann phase diagrams were successfully plotted for the first time for substituting cations with stoichiometric factors greater than unity. These diagrams allow for the prediction of solubilities across any solid solution composition, including co-substitutions in both the cation and anion sublattices as represented for the first time by a quaternary Lippmann diagram. The results illustrate that substitution of Ca by Sr increases the solubility of the resulting solid solutions under short-term metastable (stoichiometric) solubility conditions and may lead to preferential Sr release under long-term thermodynamic equilibrium conditions. These findings provide significant environmental implications for Sr-90 radionuclide immobilization using apatite-type minerals.

1. Introduction

Apatite is a versatile mineral supergroup characterized by its structure involving both cation- and anion-exchange sites capable of incorporating over half of the elements in the periodic table. This apatite supergroup includes more than 200 individually named minerals (Hughes and Rakovan, 2015). The general formula for apatite-type minerals, M_5Y_3X, where M is a divalent cation such as calcium (Ca) or strontium (Sr), Y is a trivalent oxyanion such as phosphate (PO_4^{3-}), and X is a monovalent halogen anion such as fluoride (F^-) or the hydroxyl (OH^-) anion, reflects its compositional variability. The crystal structure allows for extensive cationic and anionic substitutions on these three distinct sublattice sites, resulting in a wide range of compositional variations. However, most research has yet focused on the endmember solubilities of cationic substitutions, where divalent cations such as Sr^{2+} can replace Ca^{2+} at the related structural positions (e.g., Magalhães and Williams, 2007; Rakovan and Pasteris, 2015; Drouet, 2015). Apatite's resistance to leaching renders it an attractive host for sequestering critical radionuclides, particularly the bone-seeking fission product ^{90}Sr, which pose significant health risk due to its bone cancer triggering activity. This has increasingly led to interest in using apatite for immobilizing Sr in radioactive waste repositories and mitigating contamination at accident sites such as Chernobyl or Fukushima (Ewing and Wang, 2002; Rigali et al., 2016; Macerata et al., 2018; Robinson et al., 2023). Despite its promise, a reliable aqueous solubility model for Sr-bearing Ca apatite remains elusive, with few but often-cited experimental studies

E-mail address: kersten@uni-mainz.de.

https://doi.org/10.1016/j.apgeochem.2025.106323
Received 24 January 2025; Received in revised form 18 February 2025; Accepted 19 February 2025
Available online 24 February 2025

providing limited insights (e.g., Pan et al., 2009). In particular, the development of a solid-solution aqueous-solution (SSAS) equilibrium model is critical for evaluating environmental remediation activities.

In the present study, a series of $(Sr_xCa_{1-x})_5(PO_4)_3(OH,F)$ solid solutions with varying $x = Sr/(Ca + Sr)$ molar ratios were synthesized using a hydrothermal precipitation method, producing apatites with a hexagonal structure. If substitution were limited to a 1:1 cationic exchange at the octahedral sublattice position with no additional substitutions at the other sublattice sites (e.g., no hydroxyl by halides), the system could be described using a simple single-site binary mixing model. This model aligns with traditional SSAS frameworks, which are commonly implemented in popular thermodynamic equilibrium codes such as PHREEQC. For ternary SSAS systems, this approach is generally restricted to substitutions at a single lattice site of the structure (Rodríguez-Galán and Prieto, 2018). Alternatively, the home-brew "Nanokin" code may consider substitution at two cation sites but is limited to three endmembers only (Noguera et al., 2012). To address the intricacies of apatite-type minerals, a more sophisticated sublattice SSAS mixing model is required, particularly for systems involving complex co-substitutions of both cations and anions.

The double-co-substituting system $(Sr_xCa_{1-x})_5(PO_4)_3(OH_y,F_{1-y})$ can be conceptualized as a 2D plane where the opposing edges represent the two sublattice systems, Ca/Sr and OH/F, and the corners denote the four endmembers. The edges and diagonals then correspond to the six possible binary systems within this framework. The objective of this study was to develop a thermodynamic framework to model these complex interactions. The hypothesis driving this research was that such a model could simultaneously interpret the effects of Ca–Sr substitution at the cationic lattice site and fluoride-hydroxyl substitution at the monovalent anionic site on the aqueous solubilities of these apatite supergroup minerals. Establishing a reliable thermodynamic database is critical not only for environmental and medical applications, such as radionuclide sequestration or biomimetic bone scaffolding, but also for broader applications such as archaeological studies (Keenan, 2023). This model will thus provide valuable insights into the solubility and stability of apatite-type minerals across various both geochemical and practical domains.

2. Experimental methods

2.1. Solids preparation

The crystalline structure of apatite is influenced by both synthesis method and the temperature of formation. At room temperature, apatite typically forms monoclinic crystals (structure $P2_1/b$), whereas under hydrothermal conditions, apatite adopts a hexagonal $P6_3/m$ structure (van Rees et al., 1973). The symmetry difference arises from variations in the positioning of the hydroxyl or halogen anions within the structural channels, without significant rearrangement of the other ions. Consequently, the energetic differences between these two symmetries are minimal but not negligible (Puzio and Manecki, 2022). Given these structural considerations, a hydrothermal ageing procedure at 200 °C was chosen for synthesizing the apatite solid solutions. For this study, hexagonal-structured solid solutions of $(Ca,Sr)_5(PO_4)_3OH$ or $(Ca,Sr)_5(PO_4)_3F$ were prepared following protocols established by Onda et al. (2008) and Frangopol et al. (2016). On the other hand, the synthesis of mixed fluor-hydroxylapatite solid solutions was avoided. This decision was because of the tendency of fluoride ions to adsorb onto the surfaces of the fine precipitates during the synthesis process. If at all measurable, the total dissolved F concentrations are then more indicative of a system at saturation with nearly pure fluorapatite rather than a mixed fluor-hydroxylapatite (Tacker and Stormer, 1989).

High purity chemicals (MERCK reagent grade) and pre-boiled, deionized water were utilized in both synthesis and dissolution experiments. Precautions were taken to maintain controlled conditions and minimize CO_2 contamination. For fluorapatites, syntheses were initiated at acidic pH values (~4), while for hydroxylapatites, all solutions were purged of CO_2 by argon bubbling to prevent the incorporation of carbonate ions, which apatite readily absorbs from the atmosphere (Pan and Darvell, 2010). These precautions were sufficient to prevent formation of carbonate-bearing apatite as confirmed by FTIR and Raman spectroscopy (Solecka et al., 2025). Nitrate salts were used as precursors to avoid unwanted chloride incorporation or the precipitation of secondary sulphate phases. Two solutions were prepared for the precipitation process. Solution A contained $Ca(NO_3)_2{\bullet}4H_2O$ and/or $Sr(NO_3)_2{\bullet}4H_2O$ (33.4 mmol) in 80 mL of deionized water. Solution B contained phosphate (20 mmol) using $Na_3PO_4{\cdot}10H_2O$ in 70 mL with an excess amount of NaOH (14 mmol) or a stoichiometric amount of NaF (6.7 mmol). Solution B was thoroughly homogenized by argon bubbling before mixing with Solution A at room temperature. The molar Ca/P ratio of the combined solution was thus maintained at 1.67. The resulting suspension was transferred into a 300 mL stainless-steel batch reactor lined with Teflon (Berghof DB-300, Eningen, Germany). The reactor was equipped with a NiCr/Ni temperature sensor and heated on a hot plate (Berghof BLH-650/BAH-300) controlled by a data logger (Berghof BTC-3000). The solution was stirred and maintained under hydrothermal conditions at 200 °C overnight (14 h). For the hydroxylapatite syntheses, maintaining high pH above 10 was crucial to avoid incongruent precipitation of β-$SrHPO_4$, which could alter solubility behaviour (Verbeeck et al., 1981). After the hydrothermal treatment, the resulting precipitate was washed twice with deionized water followed by centrifugation (4700 g for 20 min). The separated precipitate was dried at 60 °C overnight.

2.2. Solids characterization

Phase purity of the samples was determined using X-ray powder diffraction (XRD). The XRD analysis was performed using a Seifert XRD 3000 TT instrument (Seifert, Ahrensburg, Germany). The instrument setup included an automatic divergence slit, a 0.02 radian primary beam Soller collimator, a diffracted beam graphite monochromator, a 0.2 mm receiving slit, and a scintillation counter. A long-fine focus Cu Kα radiation tube operated at 30 kV and 45 mA was used for the analysis. Scans were performed in stepscan mode over the range of 5–70°2θ with a step size of 0.015°2θ s^{-1}. Internal calibration was carried out using a silicon standard (silicon powder, 99.99% pure). Mineral identification, determination of crystal lattice parameters, and Rietveld compositional analysis were performed by comparing the measured XRD patterns with a reference database. The BGMN open-source code with the Profex 5.2 GUI (Döbelin and Kleeberg, 2015) was used for these analyses. Lattice parameters were calculated for the hexagonal system $P6_3/m$. Crystallite size was refined anisotropically, and the Sr content substituting Ca was parameterized to account for variable Ca/Sr elemental ratios. An example Profex file illustrating these parameterizations is provided by Table S1 of the Supporting Material.

The specific surface areas of the samples were determined using a Quantachrome NOVA 1200 system (Anton Paar, Graz, Austria), following the common Brunauer-Emmett-Teller (BET) method. Prior to the measurement, the sample powders were degassed overnight at 60 °C. To analyse the chemical composition of the samples before the dissolution experiments, approximately 100 mg of the sample was dissolved in 25 mL of 1 M HNO_3 solution (Merck Ultrapure). The solution was then diluted to 100 mL with deionized water. Concentrations of Sr and P were determined using inductively coupled plasma mass spectrometry (ICP-MS) with a triple-quad instrument (Agilent 8900, Karlsruhe, Germany). Calibration was performed using internal aqueous standards, achieving an analytical precision better than 2 % based on replicate analyses. The within-run and between-run coefficients of variation (CV) were both <3 % for all measured concentrations. Ca concentrations were determined by inductively coupled plasma optical emission spectroscopy (ICP-OES) using a Spectro Arcos instrument (Spectro Analytical Instruments, Kleve, Germany). This method was

selected to avoid interference from $^{86}Sr^{2+}$ and $^{88}Sr^{2+}$ ions occurring in the ICP-MS measurements. The detection limits were 1 μg L^{-1} for P and 0.02 μg L^{-1} for Ca and Sr, based on blank measurements. Since the solutions contained no interfering chloride ions, F^- anion concentrations were analysed using ion chromatography (Metrohm 930 Compact IC Flex instrument, Switzerland) with a detection limit of 10 μg L^{-1}.

2.3. Dissolution batch experiments

For the dissolution experiments, 100 mg of each dry powder sample was placed into a series of 50-mL centrifuge polypropylene tubes, each containing 25 mL of a 0.01 M HNO_3 solution (pH 2). All experiments were performed in triplicate at 25 °C. The solution pH was not buffered, allowing for changes over time. The suspension tubes were sealed and agitated on a horizontal mechanical shaker at a rate sufficient to prevent settling of the suspension for up to 500 h. From each triplicate tube series, one tube was sampled at 170 h, 340 h, and the last one at 500 h. The pH values were monitored at these intervals, as well as earlier in the experiment run, using a pH meter equipped with a SenTix81 combination electrode and a temperature probe (Inolab Level 2P, WTW, Weilheim, Germany). Calibration was performed at 25 °C using CertiPur buffer solutions (Merck, pH 4.01, 7.00, and 9.00). After the dissolution experiments were completed, the supernatant solutions were recovered by centrifugation at 4700*g* for 20 min. The solutions were filtered using 0.20 μm membrane filters and kept refrigerated until solute analysis. Total dissolved F, Ca, P, and Sr were analysed using again ion chromatography and ICP-OES or ICP-MS.

3. Results

3.1. Solid phase characterization

The synthesis yielded fine-crystalline, white powders exhibiting relatively sharp XRD peaks (Figs. S1 and S2). Despite good crystallinity, the BET surface areas ranged from 13 ± 1 m^2 g^{-1} for the CaPF sample to as high as 51 ± 5 m^2 g^{-1} for the SrPH sample (Table 1). All samples exhibited the same crystal structure and phase, with no evidence of impurity phases detected in the XRD patterns. The reflections confirmed the formation of monophasic apatite with a hexagonal space group $P6_3/m$. However, there were slight differences in peak locations, peak width, and absolute intensity among the diffraction patterns (Figs. S1 and S2). The diffraction peak for the 211 plane is shifting to lower 2θ value with increasing Sr content (top to bottom in Figs. S1 and S2) and the peak 112 merges with 211 with the incorporation of Sr. Variations in the intensity and width of the peaks are probably due to lattice distortions by Sr substitution. The unit cell lengths of both the *a* (=*b*) and *c* axis were calculated using the Profex code. The cell volumes were calculated by $a^2 \cdot c \cdot \sin 60$. While F^- and OH^- ions have comparable radii, the incorporation of the larger Sr^{2+} cation for Ca^{2+} in the apatite structure caused notable shifts in lattice parameters. For fluorapatite, lattice axis *a* (and *b*) increased from 9.382 to 9.720 Å, and *c* from 6.886 to 7.283 Å (Table 1), aligning well with values reported for calcined Sr-fluorapatite of >99 % phase purity ($a = 9.717$ Å, $c = 7.285$ Å; Apella et al., 1989; Lelet et al., 2022). Similarly, for hydroxylapatite, shifts from $a = 9.417$ to 9.760 Å and from $c = 6.886$ to 7.281 Å were observed, similar to the shifts from $a = 9.423$ to 9.746 Å and from $c = 6.883$ to 7.256 Å reported by Frangopol et al. (2016).

3.2. Aqueous composition of the batch equilibrium dissolution experiments

The composition of the precipitates is significantly influenced by the initial molar Ca/Sr ratios in the raw solutions due to their low solubility, unless incongruent dissolution or precipitation reactions occur. The molar (Ca + Sr)/P ratios (with P representing PO_4^{-3}) in the syntheses ranged from 1.57 to 1.75 (Table 1), which is within ±0.1 units of the theoretical stoichiometric ratio of 1.67 for apatite. In the dissolution experiments, the initial hours were characterized by a steep increase in pH value. Steady-state equilibrium was effectively reached within one week, as indicated by the levelling out to nearly constant pH values (5.47 ± 0.29 for hydroxylapatite and 4.13 ± 0.26 for fluorapatite, Tables S2 and S3). This mildly acidic pH range is ideal for preventing the formation of secondary Ca/Sr-phosphates, which can form under more acidic conditions (Verbeeck et al., 1980a,b; 1981), while more alkaline conditions may lead to re-adsorption of phosphate oxyanions (Bengtsson et al., 2009). Additionally, maintaining a nearly constant pH is crucial since the speciation of oxyanions is highly sensitive to pH changes. The steady-state after a few days is further indicated by nearly identical concentrations of total dissolved Ca, Sr, P, and F in samples collected after 170, 340, and 500 h (Tables S2 and S3). The molar (Ca + Sr)/P ratios in solution ranged from 1.60 to 1.85 (Tables S2 and S3), indicating stoichiometric solubility behaviour. This consistent behaviour was observed across all total dissolved element concentrations and pH values (Tables S2 and S3).

Table 1
Characterization of the solid synthesis products.

Phase	Sample No.	(Sr+Ca)/P	X_{Sr}	BET (m^2/g)	*a*-axis (Å)	*c*-axis (Å)	Cell volume (Å^3)
(Sr, Ca) PH	1	1.65	1.0	51	9.760	7.281	601
	2	1.69	0.91 ± 0.02	43	9.724	7.240	593
	3	1.71	0.84 ± 0.01	43	9.693	7.200	586
	4	1.59	0.68 ± 0.01	52	9.650	7.153	577
	5	1.63	0.53 ± 0.01	53	9.589	7.082	564
	6	1.73	0.37 ± 0.02	41	9.552	7.027	555
	7	1.70	0.19 ± 0.02	35	9.487	6.962	543
	8	1.75	0	20	9.417	6.886	529
(Sr, Ca) PF	1	1.59	1.0	25	9.720	7.283	596
	2	1.67	0.90 ± 0.01	41	9.685	7.244	588
	3	1.63	0.78 ± 0.02	36	9.655	7.207	582
	4	1.57	0.65 ± 0.01	45	9.593	7.127	568
	5	1.72	0.54 ± 0.01	37	9.552	7.079	559
	6	1.71	0.43 ± 0.02	32	9.514	7.034	551
	7	1.75	0.21 ± 0.01	26	9.449	6.960	538
	8	1.73	0	13	9.382	6.886	525

4. Discussion

4.1. Solid composition

Understanding the behaviour of Ca^{2+} and Sr^{2+} ions in the apatite crystal structure is crucial for evaluating their substitution mechanisms and the resulting lattice relaxation effects (Pan and Fleet, 2002). The

disparity in ionic radii between Ca^{2+} (106 p.m. in 7-fold coordination) and Sr^{2+} (121 p.m. in 7-fold coordination) suggests that the incorporation of Sr^{2+} ions into the Ca-apatite crystal structure induces lattice relaxation, increasing the unit cell parameters without causing significant lattice strain. However, the apatite crystal structure actually contains two slightly different Ca sites, Ca(I) and Ca(II) (Hughes and Rakovan, 2002). Ca(I) sites, arranged in columns parallel to the OH^- channels, exhibit in fact ninefold coordination with six oxygen atoms from six PO_4^{3-} moieties forming triangles. These are tightly bound, with an additional three oxygen atoms loosely bound, yielding an average Ca(I)–O bond length of 2.55 Å. In contrast, Ca(II) sites form a staggered triangular array, surrounded by seven oxygen atoms, including one sharing an OH^- anion, and have a slightly shorter average Ca(II)–O bond length of 2.45 Å. Cations with larger ionic radii typically prefer higher coordination numbers to reduce electrostatic repulsion between adjacent anions, influenced by lattice constraints and external conditions (P/T, fluid composition, etc.). For small amounts of Sr^{2+} substitution, the spatially larger Ca(I) sites are energetically favoured due to their ninefold coordination, which minimizes substitution energy. As Sr^{2+} substitution increases, however, repulsion at the Ca(I) site causes significant enlargement of the *c*-axis length. This effect is partially mitigated by accommodating Sr^{2+} at the smaller Ca(II) site, especially under alkaline conditions where substitution energies for both sites decrease (Ressler et al., 2021; Matsunaga and Murata, 2009).

The co-substitution of OH^- by F^- anions in the apatite lattice induces specific structural changes with significant thermodynamic implications. Substitution of the larger OH^- (168 p.m.) by the smaller F^- (132 p.m.) leads to a decrease in the *a*-axis length, while no substantial change in the *c*-axis is observed. As Zhang et al. (2020) recently explained, lattice distortion due to the substitution of larger cations results in hydrogen ions arranging in interatomic spaces adjacent to oxygen ions, forming randomly oriented OH^- groups. When these OH^- groups are replaced by F^- ions, a more ordered and lower-entropy structure forms as hydrogen ions interact with surrounding F^- ions. This structural reordering enhances the thermodynamic stability of the co-substituted apatite lattice and slightly reduces solubility as the degree of F^- substitution increases. However, the practical effect on the solubility product is minimal. This is because the solubility product is orders of magnitude more sensitive to cation and oxyanion concentrations contributing to a power of three to five to the solubility product. Consequently, while F^- ion substitution improves structural stability, its influence on overall apatite solubility is relatively minor albeit significant.

The unit cell expansion shows a linear relationship with the amount of Sr incorporated in both the hydroxyl- and fluorapatite samples as shown for both the axis lengths and cell volumes in Fig. 1. The effect of cation substitution is more prominent on the *c*-axis than on the *a*-axis. Consequently, the axis a/c ratio is linear but has a negative slope with increasing Sr content (Fig. 1c). All these linear trends conform to Vegard's law (Denton and Ashcroft, 1991). The application of Vegard's law to the lattice parameters of the solid solutions forms a critical component of this study. Previous studies have also reported similar linear trends. For instance, O'Donnell et al. (2008) observed a slight preference for Sr occupancy at the Ca(II) site rather than the Ca(I) site within the apatite structure, corresponding to a linear increase in the lattice parameters for Sr-bearing Ca-hydroxylapatite. Zhu et al. (2006) also reported a slight preference of Sr^{2+} ions for the Ca(II) sites within apatite formed by hydrothermal synthesis under alkaline conditions similar as in this study. The linear relationship consistent with Vegard's law aligns well with the Ca/Sr ratios obtained from chemical analyses, confirming the successful syntheses of regular or even ideal solid solution without formation of mixing gaps as a robust foundation for subsequent dissolution experiments.

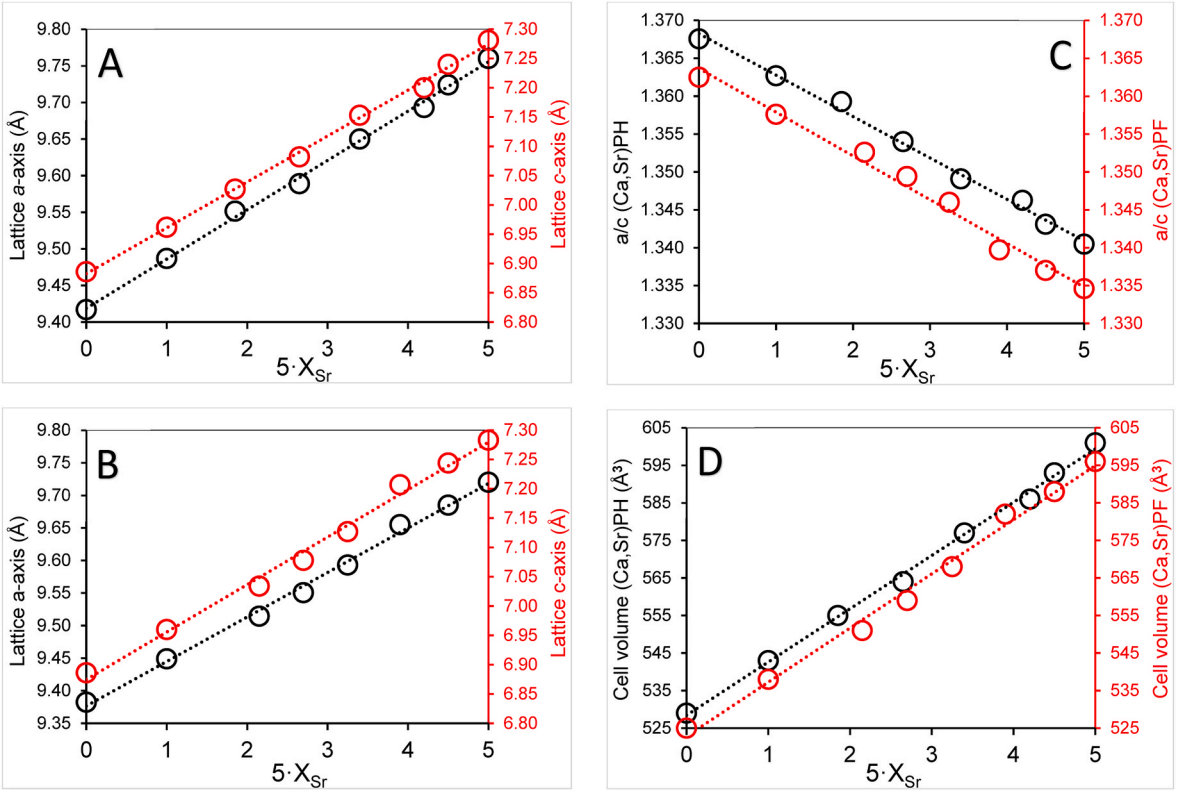

Fig. 1. Lattice axis lengths of the apatite solid solution binaries (A) CaPH – SrPH and (B) CaPF – SrPF, (C) the *a*/*c* axis ratios, and (D) the cell volumes as determined by Rietveld analysis of XRD data. The dot size equals the relatively small error range of ±0.02 Å in the axis length determinations.

4.2. Endmember solubilities

The dissolution process can be divided into distinct stages (Dorozhkin, 2014). Initially, protons from the solution interact with surface hydroxyl/fluoride ions and phosphate oxygen ions on the apatite. This interaction leads to an increase in solution pH (Zhu et al., 2009). In the next step, Ca removal occurs, involving phosphate hydrolysis and the formation of a $CaHPO_4$ layer. This process also involves the uptake of protons into the apatite structure, leading to the formation of a protonated precursor complex. Following this, hydrolysis of the remaining Ca–O bonds takes place (Chairat et al., 2007). As a result of these initial dissolution processes, the pH increased by up to three units within the first hour of the experiment. After this rapid initial reaction, the pH stabilized and remained constant for the remaining weeks of experiment duration. The system reached then a steady state, as indicated by consistent solute determinations across three consecutive measurements within the limits of analytical precision (Tables S2 and S3).

To explore the thermodynamic behaviour of the solution compositions, species distribution of the total dissolved elements was calculated at respective pH values using the Visual MINTEQ ver. 4.1 code (Gustafsson, 2022). Saturation indexes (SIs) for potential solid phases were calculated relative to their thermodynamic solubility product constants (K_{sp}) for the corresponding dissolution reactions. Solubility product constants ($\log K_{sp}$) for the CaPH endmember (H representing OH^-) were compared across various studies (Table 2). The Visual MINTEQ database lists a default $\log K_{sp}$ value of −58.3, derived from the NIST database based on an old publication (McDowell et al., 1977). This aligns with experimental data from Puzio et al. (2018), which report a $\log K_{sp}$ of −58.5, and a $\log K_{sp}$ of −58.5 theoretically predicted by an "Additive Ionic Scheme" correlation method by Drouet (2015). Some other studies have reported higher solubility for CaPH. For instance, Zhu et al. (2009) initially reported a $\log K_{sp}$ of −53.3 but later revised this to −57.65 (Zhu et al., 2016), near to the experimental value of −58.8 by Harouiya et al. (2007). Tacker and Stormer (1989) noted that thermodynamic data from hydrothermally synthesized apatite are more reliable than those from low-temperatures synthesis. Incongruent dissolution, possibly due to monetite ($CaHPO_4$) coprecipitation, may explain challenges in achieving equilibrium (Frangopol et al., 2016). After 500 h of batch dissolution experiments, the CaPH endmember (Sample #8, Table S2) exhibited a $\log K_{sp}$ of −58.2, with slight undersaturation concerning monetite (SI = −0.8). For the CaPF endmember (with F representing F^-), this study derived a $\log K_{sp}$ of −60.25 ± 0.15 (Table 2, Sample #8, Table S3), just in mid between the value of −59.9 reported by Yan et al. (2020) and −60.5 predicted by Drouet (2015). The SrPH endmember yielded a $\log K_{sp}$ of −51.55 (Table 2), nearly in agreement with the earlier value of −51.3 reported by Verbeek et al. (1977). Intriguingly, no literature data were found for the SrPF endmember. The naturally occurring pure Sr-apatite mineral stronadelphite, $Sr_5(PO_4)_3F$, is in fact quite rare. Interestingly, the solubility of SrPF appears to be 4-6 orders of magnitude higher than the corresponding Ca-apatite endmember but is supported by the reliability of our result for the SrPH endmember and by its consistency with established literature data. This indicates distinct thermodynamic properties for Sr-substituted phases, underscoring their higher solubility relative to their Ca-apatite endmembers.

4.3. Gibbs free energy of formation of the endmembers

The standard molar Gibbs energy of formation, $\Delta_f G^\circ$, so far predicted for the Ca-fluorapatite endmember, $Ca_{10}(PO_4)_6F_2$, ranges from −12830 kJ mol^{-1} (Glasser, 2022) to −12900 kJ mol^{-1} (Drouet, 2015). Experimentally derived values, including those from this study, fall within this range. For the Sr-fluorapatite endmember, $Sr_{10}(PO_4)_6F_2$, predicted values range from −12730 kJ mol^{-1} (Glasser, 2022) to −12846 kJ mol^{-1} (Jemal, 2004; Drouet, 2015). However, recently calorimetric data from

Table 2
Standard Gibbs energy of formation, enthalpy, entropy, heat capacity, and solubility product constants for the Ca/Sr apatite endmembers estimated from our own experiments, by those reported in literature where available, or calculated theoretically using the IE (Puzio and Manecki, 2022) or TAP (Drouet, 2015) approach.

Apatite	$\Delta_f G^0$ kJ mol^{-1}	$\Delta_f H^0$ kJ mol^{-1}	S^0 J K^{-1} mol^{-1}	Cp J K^{-1} mol^{-1}	$\log K_{sp}$
$Ca_5(PO_4)_3OH$	−6328 (exp.)[a]	−6655 (exp.)[b]	390 (VBT)[b]	385 (TAP)	−58.20 ± 0.25 (exp.)[a]
	−6245 (exp.)[b]	−6653 (exp.)[c]	388 (exp.)[c]	347 (MD)[e]	−57.9 (exp.)[b]
	−6255 (exp.)[c]	−6693 (exp.)[d]	398 (TAP)		−57.5 (exp.)[f]
	−6319 (exp.)[d]	−6700 (RSC)[e]	390 (MD)[e]		−59.0 (TAP)
	−6317 (TAP)	−6686 (TAP)			
		−6654 (IE)			
$Ca_5(PO_4)_3F$	−6465 (exp.)[a]	−6773 (exp.)[c]	385 (VBT)[b]	376 (TAP)	−60.25 ± 0.15 (exp.)[a]
	−6390 (exp.)[b]	−6838 (exp.)[d]	385 (TAP)	323 (MD)[e]	58.9[b]
	−6391 (exp.)[c]	−6799 (exp.)[e]			−59.9 (exp.)[g]
	−6473 (exp.)[d]	−6725 (exp.)[g]			−60.5 (TAP)
	−6450 (TAP)	−6799 (TAP)			−58.7 (IE)
		−6775 (IE)			
$Sr_5(PO_4)_3OH$	−6346 (exp.)[a]	−6687 (exp.)[c]	384 (VBT)[b]	470[h]	−51.55 ± 0.25 (exp.)[a]
	−6294 (exp.)[b]	−6689 (TAP)	470 (TAP)		−51.3 (exp.)[i]
	−6293 (TAP)	−6682 (IE)			
$Sr_5(PO_4)_3F$	−6487 (exp.)[a]	−6802 (exp.)[c]	383 (VBT)[b]	406[j]	−54.25 ± 0.15 (exp.)[a]
	−6423 (exp.)[c]	−6861 (RSC)[j]	470[j]		
	−6500 (RSC)[j]	−6802 (TAP)	456 (TAP)		
	−6423 (TAP)	−6810 (IE)			

[a] Experimental batch equilibrium data from this study.
[b] Experimental data or VBT correlations by Puzio et al. (2018, 2022, 2025).
[c] Calorimetric data by Jemal et al. (1995, 2004).
[d] Experimental batch equilibrium data by Tacker and Stormer (1989).
[e] Reaction-solution calorimetry (RSC) data and molecular dynamics (MD) calculations by Cruz et al. (2005a,b).
[f] Experimental batch equilibrium data by Verbeeck et al. (1980a,b).
[g] Experimental batch equilibrium data by Yan et al. (2020).
[h] For a first approximation assessed as equal to S^0.
[i] Experimental batch equilibrium data by Verbeeck et al. (1981).
[j] Reaction-solution calorimetry (RSC) data by Lelet et al. (2022).

Lelet et al. (2022) suggest a higher value of −13000 kJ mol^{-1}. The experimental value derived from this study can be calculated as follows:

$$\begin{aligned}\Delta_f G^0\left[Sr_5(PO_4)_3F\right] &= 5\Delta_f G^0\left(Sr^{2+}\right) + 3\Delta_f G^0\left(PO_4^{3-}\right) + \Delta_f G^0(F^-) \\ &\quad + 5.708 \cdot \log K_{sp} \\ &= 5(-563.9) + 3(-1025.1) - 281.5 - 309.7 \\ &= -6487\ kJ\ mol^{-1} \end{aligned} \quad (1)$$

from which the value of −12974 kJ mol^{-1} for $Sr_{10}(PO_4)_6F_2$ aligns more closely with the calorimetric results of Lelet et al. (2022) than with the theoretical calculations. The $\Delta_f G^0$ values for the other apatite phases were similarly calculated using thermodynamic data for the respective ions (Table S4) and are compiled in Table 2. A further significant finding

by Lelet et al. (2022) relates to the Gibbs energy of reaction for complete Ca-to-Sr substitution according to the cation exchange reaction:

$$Ca_{10}(PO_4)_6F_2 + 10Sr(NO_3)_2 = Sr_{10}(PO_4)_6F_2 + 10Ca(NO_3)_2 \quad (2)$$

Values of −13000 kJ mol^{-1} for the Sr-endmember and −12983 kJ mol^{-1} for the Ca-endmember (and values for the nitrate salts as listed in Table S4) yield in a Δ_rG° of 398 kJ mol^{-1} for this ion exchange reaction. The value for the Ca-endmember appears to be a bit too high in comparison to previous literature data (Table 2). Anyway, the positive Δ_rG° value indicates that the ion exchange reaction is not thermodynamically spontaneous, reinforcing the greater stability of the Ca-form over the Sr-form. These findings confirm that Ca-hydroxyl- or -fluorapatites are more stable thermodynamically than the respective Sr-apatites. This stability difference is critical for understanding the thermodynamic (and kinetic: Chairat et al., 2007) behaviour of these apatite phases, especially in systems involving cation substitutions and their impact on material properties.

4.4. Construction of Lippmann diagrams for the binary SSAS subsystems

The formation of a substitutional solid solution requires an excess free energy change, ΔG^{ex}, as discussed by Prieto et al. (2016, 2016). This is usually composed of a term ΔG^{mix} as the difference between the free energy of the solid solution and a compositionally equivalent mechanical mixture of the pure endmembers, and a term $\Delta G^{mix,ideal}$ as the difference between the free energy of the solid solution and the free energy of mixing of an equivalent ideal solid solution, as expressed by:

$$\Delta G^{ex} = \Delta G^{mix} - \Delta G^{mix,ideal} \quad (3)$$

In fact, the Sr-bearing apatite phases dissolved stoichiometrically (Tables S2 and S3). For practical purposes, the concept of the "stoichiometric" solubility product has been introduced to account for such cases of stoichiometric solubility behaviour (Thorstenson and Plummer, 1977; Glynn and Reardon, 1990; Prieto, 2009; Königsberger, 2013). However, the stoichiometric solubility product constants represent a metastable condition rather than a true thermodynamic equilibrium state. Under this concept, the solid solution is treated as a stoichiometric phase, just as the respective endmember phases, i.e., as a pure single-component solid with a fixed formula. This phase dissolves stoichiometrically with a stoichiometric solubility product K_{st} at the point of stoichiometric saturation of the aqueous phase relative to the solid solution. Such stoichiometric saturation, characterized by the stoichiometric dissolution of the solid solution, is commonly observed in low-solubility phases such as apatites (e.g., Pan et al., 2009; Solecka et al., 2025). Once this initial saturation is reached, the aqueous phase can remain metastable with respect to the solid solution at this stoichiometric saturation. This persistence occurs because the solid (or at least its surface) must undergo a dissolution-recrystallization process to reach true equilibrium. The kinetics of this process can be quite sluggish as already shown by Zhu et al. (2016) for the Ca–Cd apatite SSAS systems aged for over a year. Similarly, Solecka et al. (2025) observed stoichiometric dissolution and hence stoichiometric saturation in the vanadinite-mimetite SSAS system even after more than one year of aging in aqueous suspension. Stoichiometric saturation for solid solutions corresponds to equal molar Gibbs energy functions of the solid and aqueous phases, which can be represented by an "equal-G curve" (EGC) in Lippmann diagrams. The EGC curves can be derived from the conditions for metastable equilibrium as follows (Lippmann, 1980; Königsberger, 2013):

$$\Sigma K_{EGC} = X_{Sr}\cdot\ln K_{Sr} + (1 - X_{Sr})\cdot\ln K_{Ca} + \Delta G^{mix}/RT \quad (4)$$

where K_{Sr} refers to the endmember solubility product of the SrPH or SrPF apatite, K_{Ca} to the endmember solubility product of the CaPH or CaPF apatite, R is the ideal gas constant, and T is the temperature in Kelvin. The stoichiometric solubility product constants K_{st} were calculated for each of the dissolution experiment (Tables S2 and S3, the original logK_{st} values were divided by a factor of 5 to fit to the 1/5ΣΠ curves in the Lippmann diagrams as discussed below). As shown in Fig. 2a and b by the blue dots and lines, there is no deviation of the thus recalculated experimental points from the straight EGC line connecting the endmember solubility product constants. The excess Gibbs energy of mixing in the solid phase, ΔG^{mix}, is therefore zero indicating ideal mixing in the solid solution according to equation (3), i.e., $\Delta G^{ex} = \Delta G^{mix,ideal}$. Similar as found by Pan et al. (2009), the apatite stoichiometric solubility significantly and linearly increased with the increase of Sr content. The remaining ideal Gibbs energy of mixing can then be calculated from the configurational entropy:

$$\Delta G^{mix,ideal} = -T\cdot\Delta S^{mix,ideal} = RT(X_1\cdot\ln X_1 + X_2\cdot\ln X_2) \quad (5)$$

The thermodynamic equilibrium in binary solid solution systems is described by the equivalence of the standard chemical potentials and activity terms of the solid and aqueous phase components. For the hypothetical hydroxylapatite endmember, these may in turn be recalculated to the respective solubility product constant, $K_{MYZ} = \{M^{2+}\}^5\{Y^{3-}\}^3\{Z^-\}$, where the curly braces denote aqueous ion activities, and by the respective law of mass action expressions:

$$\left\{M^{2+}\right\}^5\left\{PO_4^-\right\}^3\{Z^-\} = K_{sp,MPZ}X_{MPZ}\,\lambda_{MPZ} \quad (6)$$

The solid-phase activities in a binary are given as the product of their respective mole fractions, $X_{i,j}$, and activity coefficients, $\lambda_{i,j}$. Alternatively, another expression for the thermodynamic SSAS equilibrium is obtained by simply adding the two mass action law expressions (6) to give, for example, for the CaPH–CaPF SSAS system:

$$\begin{aligned}\Sigma\Pi_{eq} &= \left\{Ca^{2+}\right\}^5\left\{PO_4^-\right\}^3(\{OH^-\} + \{F^-\}) \\ &= \left(K_{sp,CaPH}X_{CaPH}\lambda_{CaPH}\right) + \left(K_{sp,CaPF}X_{CaPF}\lambda_{CaPF}\right)\end{aligned} \quad (7)$$

The left term in Eq. (7) contributes the so-called Lippmann's "total ion activity product" variable ΣΠ, which is fixed by the right term to the "total solubility product" constant $\Sigma\Pi_{eq}$ at thermodynamic equilibrium (Lippmann, 1980; Glynn and Reardon, 1990; Prieto et al., 2016). The $\Sigma\Pi_{eq}$ constant can be calculated if the individual activities of the endmember components in the solid phase (λ_{CaPH} and λ_{CaPF}) at thermodynamic equilibrium are known. Alternatively, $\Sigma\Pi_{eq}$ can be calculated if the activity fractions of the substituent ions in the aqueous phase at thermodynamic equilibrium are known. For an ideal mixing ($\lambda = 1$) it follows:

$$\log\Sigma\Pi_{eq} = \log\left[(1 - X_{CaPH})\left(K_{sp,CaPH}\right) + X_{CaPF}\left(K_{sp,CaPF}\right)\right] \quad (8)$$

The aqueous solute activity fractions for this SSAS system are defined in turn by:

$$\chi_{OH,aq} = \{OH^-\} / (\{OH^-\} + \{F^-\}) \quad (9)$$

and

$$\chi_{F,aq} = \{F^-\} / (\{OH^-\} + \{F^-\}) \quad (10)$$

Substituting these two equations into the total solubility product and rearranging by expressing the activities of the solid-phase components in terms of their activity coefficients and mole fractions gives finally another expression for the total solubility product by:

$$\Sigma\Pi_{eq} = \frac{1}{\frac{\chi_{OH,aq}}{K_{sp,CaPH}\lambda_{CaPH}} + \frac{\chi_{F,aq}}{K_{sp,CaPF}\lambda_{CaPF}}} = \frac{K_{sp,CaPF}\lambda_{CaPF}}{\left[1 - \chi_{OH,aq}\left(1 - \frac{K_{sp,CaPF}\lambda_{CaPF}}{K_{sp,CaPH}\lambda_{CaPH}}\right)\right]} \quad (11)$$

Note that the activity coefficients $\lambda_{CaPH} = \lambda_{CaPF} = 1$ can be neglected for ideal SSAS systems. Since $K_{sp,CaPF} \ll K_{sp,CaPH}$, Eq. (11) can be approximated by $\log\Sigma\Pi_{eq} = \log K_{sp,\,CaPF} - \log\chi_{F,aq}$. Eqs. (8) and (11) are plotted as an ordinate simultaneously against the solid solution mole fraction abscissa X_{CaPF} to give the Lippmann's "*solidus*" curve, and

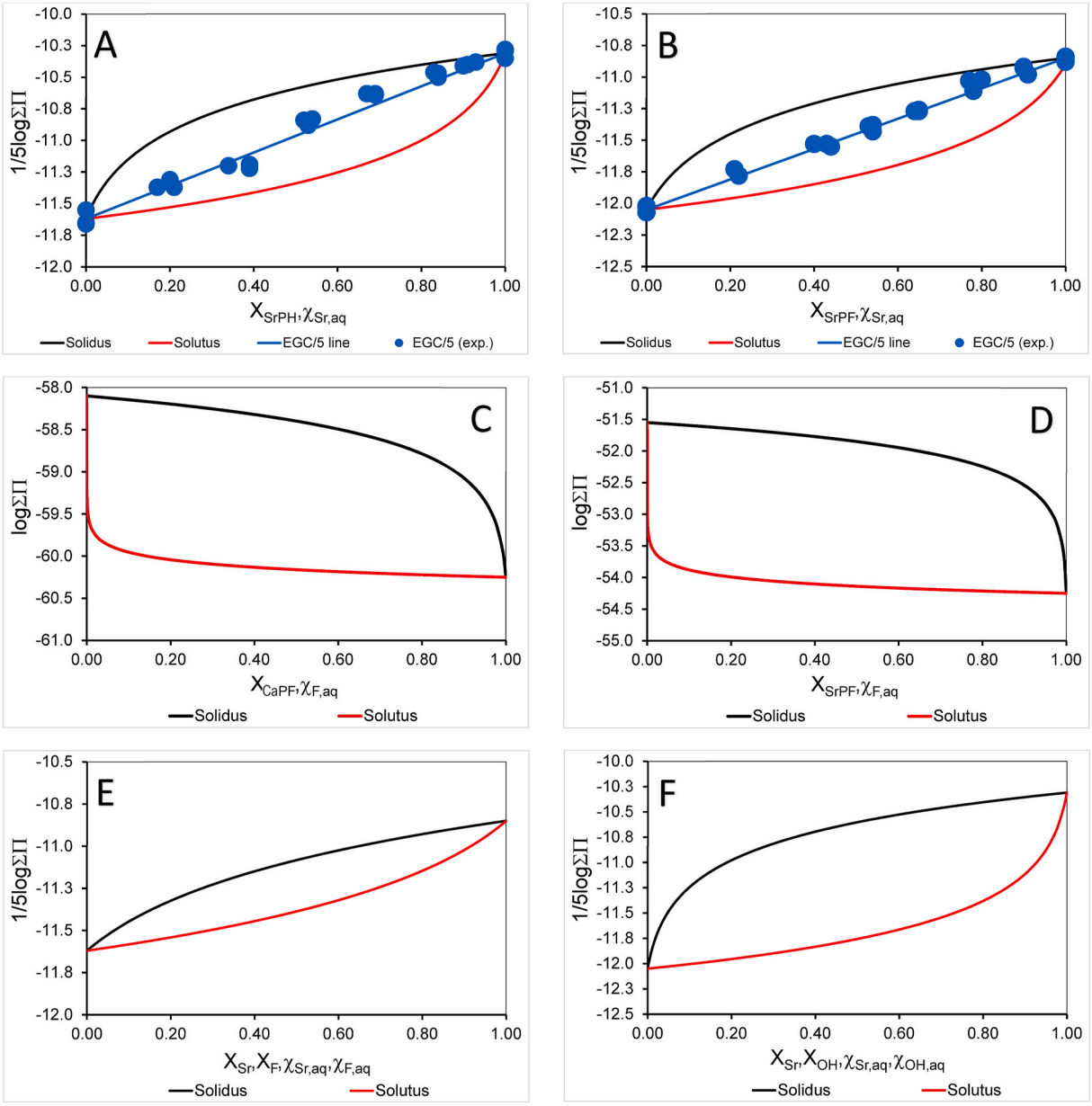

Fig. 2. Binary Lippmann plots for the total solubility product constants of the (A) CaPH – SrPH, (B) CaPF – SrPF, (C) CaPH – CaPF, (D) SrPH – SrPF, (E) CaPH – SrPF, and (F) CaPF – SrPH solid solution binaries.

against the ion activity mole fraction $\chi_{F,aq}$ to give the "*solutus*" curve calculated, e.g., by using the MBSSAS code (Glynn, 1991). This Lippmann diagram is shown for the CaPH - CaPF SSAS system in Fig. 2c, and accordingly for the SrPH - SrPF SSAS system in Fig. 2d. Unfortunately, the shape of both Lippmann curves cannot be verified by batch equilibrium experimental data due to the reasons mentioned in the methods section.

The advantage of the Lippmann total solubility product is that it allows for a straightforward comparison of the solubility product constants at the endmember compositions ($X_i = 0$ and 1). A horizontal "conode" line that intersects the solidus and the solutus curves defines the aqueous solution compositions in equilibrium with the respective solid solution composition. A notable difference in composition between those solutus and solidus points, resulting from the typical loop between these curves, corresponds to the non-stoichiometric partitioning of an ion between solid and aqueous phases at thermodynamic equilibrium. This partitioning can be defined using a distribution coefficient (K_d) value (Balter and Lécuyer, 2004). Such K_d values can be predicted using our SSAS approach. The shape of the solutus curves in the Lippmann diagrams highlights a significant fluoride enrichment in the solid solutions relative to the aqueous solutions, even at low aqueous F^- concentrations. This observation has important health implications, such as the reduced solubility of tooth enamel achieved through the application of fluoride-containing toothpaste.

For the CaPF–SrPF SSAS system, the Lippmann equations become more complicated because the cation activities count to the power of five:

$$\begin{aligned} \Sigma\Pi_{eq} &= \{F^-\}\{PO_4^-\}^3\left(\{Ca^{2+}\}^5 + \{Sr^{2+}\}^5\right) \\ &= \left(K_{sp,CaPF}X_{CaPF}\lambda_{CaPF}\right) + \left(K_{sp,SrPF}X_{SrPF}\lambda_{SrPF}\right) \end{aligned} \quad (12)$$

For an ideal mixing ($\lambda = 1$) it follows now:

$$1/5\log\Sigma\Pi_{eq} = log\left[(1 - X_{SrPF})\left(K_{sp,CaPF}\right)^{1/5} + X_{SrPF}\left(K_{sp,SrPF}\right)^{1/5}\right] \quad (13)$$

because K_{sp} refers to five cation groups in the respective endmember stoichiometries. However, since the $K_{sp,CaPF} \ll K_{sp,SrPF}$ by six orders of magnitude, this equation can conveniently be approximated by (except maybe at very low $X_{SrPF} < 10^{-3}$ which cannot be resolved in the diagram):

$$1/5 log\Sigma\Pi_{eq} = 1/5 \log K_{sp,SrPF} + \log X_{SrPF} \quad (14)$$

The aqueous solute activity fractions for the SSAS system CaPF - SrPF are accordingly defined by:

$$\chi_{Ca,aq} = \{Ca^{2+}\}^5 \; / \; \left(\{Ca^{2+}\}^5 + \{Sr^{2+}\}^5\right) \quad (15)$$

and

$$\chi_{Sr,aq} = \{Sr^{2+}\}^5 \; / \; \left(\{Ca^{2+}\}^5 + \{Sr^{2+}\}^5\right) \quad (16)$$

It is important to note that previous attempts to present accurate Lippmann diagrams for cations with a stoichiometric coefficient greater than unity were unsuccessful. For example, Zhu et al. (2016) plotted the Lippmann solutus curve for the $(Cd_xCa_{x-1})(PO_4)_3OH$ SSAS system based on $\chi_{Cd,aq} = \{Cd^{2+}\}^5/(\{Cd^{2+}\} + \{Ca^{2+}\})^5$, which is incorrect as already discussed by Königsberger (2013). The difference is significant for the comparable total dissolved Ca and Sr concentrations (Tables S2 and S3). At the slightly acidic pH values of the diluted batch equilibrium solutions, the free cation activities are nearly equivalent to the total dissolved concentrations of both elements. For instance, at an $X_{SrPF} = 0.5$, the correct value for $\chi_{Sr,aq} = \{Sr^{2+}\}^5/(\{Ca^{2+}\}^5+\{Sr^{2+}\}^5)$ is 0.96 (Table S3), while a $\chi_{Sr,aq} = \{Sr^{2+}\}^5/(\{Ca^{2+}\}+\{Sr^{2+}\})^5$ would yield in an incorrect value of 0.12. According to the Conode concept, the $\chi_{Sr,aq}$ value should be greater than that for X_{SrPF} (Fig. 2b). By substituting the correct equations into the total solubility product and rearranging the terms to

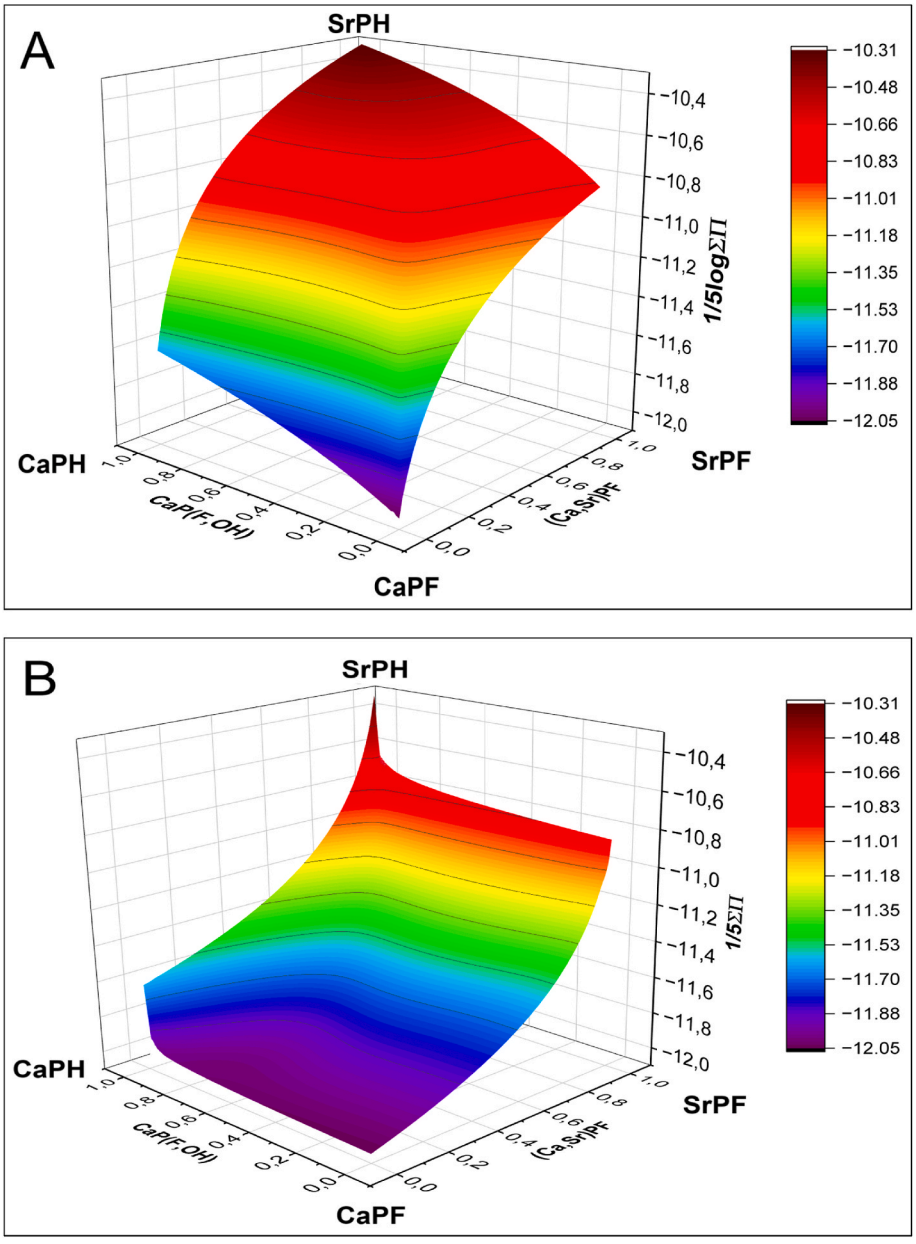

Fig. 3. Quaternary Lippmann plots for the total solubility product constants with (A) the solidus and (B) the solutus planes of the CaPH – CaPF – SrPH – SrPF solid solution system. The plots are interpolated from two ternary diagrams around the (Ca,Sr)P(F,OH) system (Fig. 2f) as diagonal line. The $1/5\log\Sigma\Pi_{eq}$ values are color-coded identically in both (A) and (B) for better visualization.

express the activities of the solid-phase components in terms of their activity coefficients and mole fractions, we arrive finally at an alternative expression for the total solubility product of the *solutus* curve:

$$1/5log\Sigma\Pi_{eq} = log\left(\frac{1}{\frac{\chi_{Ca,aq}}{\left(K_{sp,CaPF}\lambda_{CaPF}\right)^{1/5}}+\frac{\chi_{Sr,aq}}{\left(K_{sp,SrPF}\lambda_{SrPF}\right)^{1/5}}}\right)$$

$$= log\left(\frac{\left(K_{sp,CaPF}\lambda_{CaPF}\right)^{1/5}}{1-\chi_{Sr,aq}\left(1-\frac{\left(K_{sp,CaPF}\lambda_{CaPF}\right)^{1/5}}{\left(K_{sp,SrPF}\lambda_{SrPF}\right)^{1/5}}\right)}\right) \quad (17)$$

Note that the activity coefficients $\lambda_{CaPF} = \lambda_{SrPF} = 1$ can again be neglected for an ideal SSAS system, and since $K_{sp,CaPF} \ll K_{sp,SrPF}$, Eq. (17) can be approximated by $1/5\log\Sigma\Pi_{eq} = 1/5\log K_{sp,\ CaPF} - \log(1 - \chi_{Sr,aq})$. Lippmann *solidus* and *solutus* equations for the CaPH - SrPH SSAS system can be established accordingly. The solidus and solutus curves for both the hydroxyl- and fluorapatite SSAS systems are plotted in Fig. 2a and b. The correct Lippmann diagram for the SSAS system CdPH–CaPH studied by Zhu et al. (2016) has been recalculated and is shown in Fig. S4.

After separately setting up the binary Lippmann diagrams for the cation and anion systems, binary Lippmann diagrams for the mixed cation/anion systems can now be plotted. Fig. 2e and f presents exemplary Lippmann diagrams for the CaPH–SrPF and CaPF–SrPH solid solution binaries. In both plots, the *x*-axis represents the cation compositions X_{cat} and χ_{cat}, which are set equal the corresponding anion compositions, X_{an} and χ_{an}, respectively. Assuming a square framework formed by the four endmembers CaPH, CaPF, SrPF, and SrPH, these mixed cation/anion binaries represent the diagonals of the square. Consequently, a quaternary Lippmann diagram can be plotted for the first time ever, composed of two merged ternary systems with the (Ca,Sr)P(OH,F) binary as diagonal curve (Fig. 3a and b). The resulting *solidus* and *solutus planes* are color-coded according to the corresponding $1/5\log\Sigma\Pi_{eq}$ values. Since no experimental data are available for the mixed systems, these planes between the well-constrained bordering binary curves were interpolated using the graph surface smoothing tool in OriginPro (2025). Origin project files can be found in the Supporting Material. The plots reveal the complex SSAS equilibrium behaviour and solubilities within this quaternary apatite supergroup system with cation/anion co-substitution. As can be readily observed from that quaternary Lippmann diagram, the CaPF endmember exhibits the lowest solubility, while the SrPH endmember shows the highest solubility. Lippmann diagrams describe true thermodynamic equilibrium states, where the solid solution phases dissolve incongruently, as reflected in the widening of the loop between the *solidus* and *solutus* curves. The wider the less symmetrical are loops thus forming.

However, since true thermodynamic equilibrium could not be achieved in our experiments, none of the theoretical Lippmann curves could be directly verified by experimental data. Nonetheless, these theoretical projections remain valuable for predicting long-term solubility behavior when approaching thermodynamic equilibrium, particularly in the context of the disposal of ^{90}Sr-bearing apatite in radionuclide waste repositories. As discussed earlier, the positive $\Delta_r G^0$ value indicates that the ion exchange reaction is not thermodynamically spontaneous and therefore less favorable. Together with the overall low solubility, this hindrance might be the main reason for the sluggish reaction kinetics leading to stoichiometric saturation rather than thermodynamic equilibrium. If thermodynamic equilibrium were to be approached or even reached over several years in a nuclear waste repository, the Lippmann diagrams predict that at low Sr content in the solid phase (represented by small X_{SrPH} or X_{SrPF} values on the black *solidus* curves in Fig. 2a and b), the corresponding $\chi_{Sr,aq}$ value would significantly increase (as shown on the red *solutus* curves in Fig. 2a and b) due to the widening of the loop between the Lippmann curves. This implies that the more an equilibrium state is approached, the more the solubility would become non-stoichiometric with preferential release of Sr. The aqueous Sr cation concentration could then surpass the Sr cation proportion in the solid apatite phase, creating conditions that are less favorable for long-term radionuclide waste containment. These theoretical predictions highlight potential challenges, although it remains uncertain whether such thermodynamic equilibrium conditions would ever be achieved within the decades only of decay timeframe of the ^{90}Sr radionuclide.

5. Conclusions

In this study, correct Lippmann diagrams are presented for the first time for a solid solution–aqueous solution equilibrium, where the stoichiometry of the co-substituting cations exceeds unity. This approach was successfully applied to predict the aqueous solubilities of solid solutions within the apatite system $(Ca,Sr)_5[(PO_4]_3(OH,F)$, comprising four endmembers. Additionally, a stoichiometric saturation model was fine-tuned through parameterization using a series of experimental solubility data at 25 °C. This core apatite model, incorporating both true thermodynamic equilibria as represented by the Lippmann equations/curves and metastable stoichiometric saturation states, with all its thermodynamic parameters optimized and fixed, not only enables predictions of solubilities for intermediate solid solution compositions but also establishes a foundation for incremental and consistent extensions to include endmembers containing cations beyond those studied here, e.g., toxic trace elements such as Cd. Such extensions are of interest for environmental applications. Achieving true thermodynamic equilibrium, as represented by the Lippmann diagrams, may require experimental aqueous suspension aging for years. However, from a practical perspective, a "quick-and-dirty" metastable equilibrium is often more relevant for evaluating environmental remediation activities. Conversely, the accurate Lippmann diagrams presented here for the first time for Sr-bearing apatite are primarily of interest for long-term ^{90}Sr-bearing radionuclide waste storage because of the 28.5 years half-life of that bone-seeking fission product. The solubility of the Ca-apatite endmember is significantly lower than that of the Sr-apatite endmember. Consequently, Ca is preferentially incorporated over Sr into the solid solution. The shape of and loop between the *solidus* and *solutus* curves in the Lippmann diagrams highlights a significant Sr enrichment in the aqueous solutions relative to the solid solutions at thermodynamic equilibrium, even at low solid Sr concentrations. In summary, this study reaffirms that experimental apatite SSAS systems are characterized by a metastable stoichiometric equilibrium rather than a true thermodynamic one. In a forthcoming contribution, we will therefore move away from the batch dissolution equilibration approach and instead employ acid-solution calorimetry to demonstrate how this double co-substituting SSAS system can be even extended to a triple co-substituting system by additionally substituting phosphate on the oxyanion sublattice site.

Declaration of competing interest

The authors declare that they have no known competing financial interests or personal relationships that could have appeared to influence the work reported in this paper.

Acknowledgment

The project was financed with resources of the German National Science Foundation (Grant No. DFG KE 508-31). We appreciate also a Ukraine refugee fellowship grant from the Volkswagen Foundation for Nataliya Vlasova (passed away in October 2022), who helped in laboratory work with her husband Alex Baresh, together with Carolin Berg, Gerlinde Borngässer, and Regina Walter. Ralf Meffert helped with the XRD analysis.

Appendix A. Supplementary data

Supplementary data to this article can be found online at https://doi.org/10.1016/j.apgeochem.2025.106323.

Data availability

Data will be made available on request.

References

Apella, M.C., Tuttolomondo, M.E., Baran, E.J., 1989. X-ray and spectroscopic investigation of some strontium and zinc substituted calcium fluoroapatites. Z. Naturforsch. 44b, 402–404.

Balter, V., Lécuyer, C., 2004. Determination of Sr and Ba partition coefficients between apatite and water from 5 °C to 60 °C: a potential new thermometer for aquatic paleoenvironments. Geochem. Cosmochim. Acta 68, 423–432.

Bengtsson, Å., Shchukarev, A., Persson, P., Sjöberg, S., 2009. A solubility and surface complexation study of a non-stoichiometric hydroxyapatite. Geochem. Cosmochim. Acta 73, 257–267.

Chairat, C., Schott, J., Oelkers, E.H., Lartigue, J.-E., Harouiya, N., 2007. Kinetics and mechanism of natural fluorapatite dissolution at 25 degrees C and pH from 3 to 12. Geochem. Cosmochim. Acta 71, 5901–5912.

Cruz, F.J.A.L., Minas de Piedade, M.E., Calado, J.C.G., 2005a. Standard molar enthalpies of formation of hydroxy-, chlor-, and bromapatite. J. Chem. Thermodyn. 37, 1061–1070.

Cruz, F.J.A.L., Canongia Lopes, J.N., Calado, J.C.G., Minas de Piedade, M.E., 2005b. A molecular dynamics study of the thermodynamic properties of calcium apatites. 1. Hexagonal phases. J. Phys. Chem. B 109, 24473–24479.

Denton, A.R., Ashcroft, N.W., 1991. Vegard's law. Phys. Rev. A 43, 3161–3164.

Döbelin, N., Kleeberg, R., 2015. Profex: a graphical user interface for the Rietveld refinement program BGMN. J. Appl. Crystallogr. 48, 1573–1580.

Dorozhkin, S.V., 2014. The dissolution mechanism of calcium apatites in acids. In: Lafisco, M., Delgado-López, J.M. (Eds.), Apatite: Synthesis, Structural Characterization and Biomedical Applications. Elsevier, pp. 141–172. ISBN 978-163321536-8, 978-163321500-9.

Drouet, C., 2015. A comprehensive guide to experimental and predicted thermodynamic properties of phosphate apatite minerals in view of applicative purposes. J. Chem. Thermodyn. 81, 143–159.

Ewing, R.C., Wang, L.M., 2002. Phosphates as nuclear waste forms. Rev. Mineral. Geochem. 48, 673–699. https://doi.org/10.2138/rmg.2002.48.18.

Frangopol, P.T., Mocanu, A., Almason, V., Garbo, C., Balint, R., Borodi, G., Bratu, I., Horowitz, O., Tomoaia-Cotisel, M., 2016. Synthesis and structural characterization of strontium substituted hydroxyapatites. Rev. Roum. Chem. 61, 337–344.

Glasser, L., 2022. Correction to apatite thermochemistry: the simple salt approximation. Inorg. Chem. 61, 13457–13463.

Glynn, P.D., Reardon, E.J., 1990. Solid-solution aqueous-solution equilibria: thermodynamic theory and representation. Am. J. Sci. 290, 164–201.

Glynn, P.D., 1991. MBSSAS: a code for the computation of Margules parameters and equilibrium relations in binary solid-solution aqueous-solution systems. Comput. Geosci. 17, 907–966.

Gustafsson, J.P., 2022. Visual MINTEQ Ver, 4.0. https://vminteq.com/.

Harouiya, N., Chairat, C., Köhler, S.J., Gout, R., Oelkers, E.H., 2007. The dissolution kinetics and apparent solubility of natural apatite in closed reactors at temperatures from 5° to 50°C and pH from 1 to 6. Chem. Geol. 244, 554–568.

Hughes, J.M., Rakovan, J., 2002. The crystal structure of apatite, $Ca_5(PO_4)_3(F,OH,Cl)$. Rev. Mineral. Geochem. 48, 1–12. https://doi.org/10.2138/rmg.2002.48.1.

Hughes, J.M., Rakovan, J., 2015. Structurally robust, chemically diverse: apatite and apatite supergroup minerals. Elements 11, 165–170.

Jemal, M., Ben Cherifa, A., Khattech, I., Ntahomvukiye, I., 1995. Standard enthalpies of formation and mixing of hydroxy- and fluorapatites. Thermochim. Acta 259, 13–21.

Jemal, M., 2004. Thermochemistry and relative stability of apatite phosphates. Phosphorus Res. Bull. 15, 119–124.

Keenan, S.W., 2023. Thermodynamic stabilities of apatite phases in a wetland system: implications for bone diagenesis. Appl. Geochem. 148, 105546.

Königsberger, E., 2013. Solid-solute phase equilibria in aqueous solution: fundamentals and applications. Pure Appl. Chem. 85, 2089–2095.

Lelet, M.I., Mikhailov, D.A., Lyakaev, D.V., Lelet, J.N., Fukina, D.G., 2022. A calorimetric and thermodynamic investigation of strontium fluorapatite $Sr_{10}(PO_4)_6F_2$. J. Chem. Thermodyn. 164, 106636.

Lippmann, F., 1980. Phase diagrams depicting the aqueous solubility of binary mineral systems. N. Jb. Miner. Abh. 139, 1–25.

Macerata, E., Pizzi, E., Ossola, A., Giola, M., Mariani, M., 2018. Fluorapatite as immobilization matrix for nuclear waste. Radiat. Eff. Defect Solid 173, 763–771. https://doi.org/10.1080/10420150.2018.1528602.

Magalhães, M.C.F., Williams, P.A., 2007. Apatite group minerals: solubility and environmental remediation. In: Letcher, T.M. (Ed.), Thermodynamics, Solubility and Environmental Issues, pp. 327–340. Chapter 18.

Matsunaga, K., Murata, H., 2009. Strontium substitution in bioactive calcium phosphates: a first-principles study. J. Phys. Chem. 113, 3584–3589.

McDowell, H., Gregory, T.M., Brown, W.E., 1977. Solubility of $Ca_5(PO_4)_3OH$ in the system $Ca(OH)_2$–H_3PO_4–H_2O at 5, 15, 25, and 37°C. J. Res. Nat. Bur. Stand. 81, 273.

Noguera, C., Fritz, B., Clément, A., 2012. A theoretical treatment of the precipitation of doubly substituted solid solution in aqueous solutions. Cryst. Growth Des. 12, 3444–3457.

O'Donnell, M.D., Fredholm, Y., de Rouffignac, A., Hill, R.G., 2008. Structural analysis of a series of strontium-substituted apatites. Acta Biomater. 4, 1455–1464.

Onda, A., Ogo, S., Kajiyoshi, K., Yanagisawa, K., 2008. Hydrothermal synthesis of vanadate/phosphate hydroxyapatite solid solutions. Mater. Lett. 62, 1406–1409.

Pan, H.B., Li, Z.Y., Lam, W.M., Wong, J.C., Darvell, B.W., Luk, K.D.K., Lu, W.W., 2009. Solubility of strontium-substituted apatite by solid titration. Acta Biomater. 5, 1678–1685.

Pan, Y., Fleet, M.E., 2002. Compositions of the apatite-group minerals: substitution mechanisms and controlling factors. Rev. Mineral. Geochem. 48, 13–49.

Pan, H., Darvell, B.W., 2010. Effect of carbonate on hydroxyapatite solubility. Cryst. Growth Des. 10, 845–850.

Prieto, M., 2009. Thermodynamics of solid solution-aqueous solution systems. Rev. Mineral. Geochem. 70, 47–85.

Prieto, M., Heberling, F., Rodríguez-Galán, R.M., Brandt, F., 2016. Crystallization behavior of solid solutions from aqueous solutions: an environmental perspective. Prog. Cryst. Growth Char. Mater. 62, 29–68.

Puzio, B., Manecki, M., Kwasniak-Kominek, M., 2018. Transition from endothermic to exothermic dissolution of hydroxyapatite $Ca_5(PO_4)_3OH$ – johnbaumite $Ca_5(AsO_4)_3OH$ solid solution series at temperatures ranging from 5 to 65 °C. Minerals 8, 281. https://doi.org/10.3390/min8070281.

Puzio, B., Manecki, M., 2022. The prediction method for standard enthalpies of apatites using the molar volume, lattice energy, and linear correlations from existing experimental data. Contrib. Mineral. Petrol. 177, 103.

Puzio, B., Manecki, M., 2025. Estimation of missing third-law standard entropy of apatite supergroup minerals using the optimized Volume-based Thermodynamics. Contrib. Mineral. Petrol. 180, 2.

Rakovan, J.F., Pasteris, J.D., 2015. A technological gem: materials, medical, and environmental mineralogy of apatite. Elements 11, 195–200.

Ressler, A., Žužić, A., Ivanišević, I., Kamboj, N., Ivanković, H., 2021. Ionic substituted hydroxyapatite for bone regeneration applications: a review. Open Ceramics 6, 100122.

Rigali, M.J., Brady, P.V., Moore, R.C., 2016. Radionuclide removal by apatite. Am. Mineral. 101, 2611–2619.

Robinson, C., Shaw, S., Lloyd, J.R., Graham, J., Morris, K., 2023. Phosphate (bio) mineralization remediation of ^{90}Sr-contaminated groundwaters. ACS ES&T Water 3, 3223–3234.

Rodríguez-Galán, R.M., Prieto, M., 2018. Interaction of nonideal, multicomponent solid solutions with water: a simple algorithm to estimate final equilibrium states. G-cubed 19, 1348–1359.

Solecka, U., Puzio, B., Kersten, M., Topolska, J., Manecki, M., Bajda, T., 2025. Solubility of mimetite $Pb_5(AsO_4)_3Cl$ – vanadinite $Pb_5(VO_4)_3Cl$ solid solution series at 5–65 °C. Chem. Geol. 675, 122609.

Tacker, R.C., Stormer, J.C., 1989. A thermodynamic model for apatite solid solutions, applicable to high-temperature geologic problems. Am. Mineral. 74, 877–888.

Thorstenson, D.C., Plummer, L.N., 1977. Equilibrium criteria for two-component solids reacting with fixed composition in an aqueous phase. Example: the magnesian calcites. Am. J. Sci. 277, 1203–1223.

Van Rees, H.B., Mengeot, M., Kostinger, E., 1973. Monoclinic-hexagonal transition in hydroxyapatite and deuterohydroxyapatite single crystals. Mater. Res. Bull. 8, 1307–1310.

Verbeek, R.M.H., Hauben, M., Thun, H.P., Verbeek, F., 1977. Solubility and solution behaviour of strontiumhydroxyapatite. Z. Phys. Chem (Neue Folge) 108, 203–215.

Verbeeck, R.M.H., Steyaer, H., Thun, H.P., Verbeek, F., 1980a. Solubility of synthetic calcium hydroxyapatites. J. Chem. Soc. Faraday Trans. I 76, 209–219.

Verbeeck, R.M.H., Thun, H.P., Verbeek, F., 1980b. Stability behaviour of synthetic strontiumhydroxyapatites. Z. Phys. Chem. (Neue Folge) 120, 199–210.

Verbeeck, R.M.H., Driessens, F.C.M., Thun, H.P., Verbeek, F., 1981. Stability of calcium-strontium hydroxyapatite solid solutions in aqueous solutions at 25°. Bull. Soc. Chim. Belg. 90, 409–417.

Yan, Q., Zhu, Y., Feng, G., Zhu, Z., Zhang, L., Liu, J., He, H., 2020. Characterization, dissolution and solubility of lead fluorapatite at 25-45 °C. Appl. Geochem. 120, 104659.

Zhang, X., Wang, B., Ma, L., Xie, L., Yang, H., Li, Y., Wang, S., Qiao, H., Lin, H., Lan, J., Huang, Y., 2020. Chemical stability, antibacterial and osteogenic activities study of strontium-silver co-substituted fluorohydroxyapatite nanopillars: a potential multifunctional biological coating. Ceram. Int. 46, 27758–27773.

Zhu, K., Yanagisawa, K., Shimanouchi, R., Onda, A., Kajiyoshi, K., 2006. Preferential occupancy of metal ions in the hydroxyapatite solid solutions synthesized by hydrothermal method. J. Eur. Ceram. 26, 509–513.

Zhu, Y., Zhang, X., Chen, Y., Xie, Q., Lan, J., Qian, M., He, N., 2009. A comparative study on the dissolution and solubility of hydroxylapatite and fluorapatite at 25 °C and 45 °C. Chem. Geol. 268, 89–96.

Zhu, Y., Zhu, Z., Zhao, X., Liang, Y., Dai, L., Huang, Y., 2016. Characterization, dissolution and solubility of cadmium-calcium hydroxyapatite solid solutions at 25 °C. Chem. Geol. 423, 34–48.